Available online at www.sciencedirect.com
ScienceDirect
Trans. Nonferrous Met. Soc. China 33(2023) 1472−1491
Transactions of Nonferrous Metals Society of China
www.tnmsc.cn

Wear behavior and microstructure evolution in pure nickel extrusion manufacturing

Yan-jiang WANG[1,2], Zhi JIA[1,2], Jin-jin JI[3], Bao-lin WEI[1,2], Ya-bo HENG[1,2], De-xue LIU[1,2]

1. State Key Laboratory of Advanced Processing and Recycling of Nonferrous Metals, Lanzhou University of Technology, Lanzhou 730050, China;
2. School of Material Science and Engineering, Lanzhou University of Technology, Lanzhou 730050, China;
3. School of Materials Engineering, Lanzhou Institute of Technology, Lanzhou 730050, China

Received 2 November 2021; accepted 6 April 2022

Abstract: The mechanical properties of extruded bar are dominated by its surface morphology and microstructure. In this study, field extrusion and finite element simulations were combined to study the surface wear behavior and microstructure evolution mechanism of extruded workpieces. The results showed that the extrusion temperature greatly influenced the surface morphology and microstructure. As the extrusion temperature increased, the wear mechanism changed from abrasive wear (brittle damage) to adhesive wear (plastic damage), and the surface roughness gradually increased. During the extrusion, the temperature and stress of the billet presented a gradient distribution, and the dislocation walls in the deformed grains easily moved on the activated slip system, which made the layered structure deformed. With increasing the gradient distribution of the billet and the interface friction, the layered structure became narrower. The orientation gradient of geometrically necessary dislocations in the deformed grain also dominated the five strong ideal textures. These findings provide theoretical support for the precise extrusion of pure nickel and nickel alloys.

Key words: pure nickel; warm extrusion; wear mechanism; layered structure

1 Introduction

With the increase of the demand for comprehensive performances, the accuracy of microstructure and surface quality have drawn more attention during hot extrusion. Much research has been conducted to identify methods to control surface defects and microstructures during the extrusion of lightweight alloys such as those of aluminum [1] and titanium [2]. However, there are few studies on the surface defects and microstructure of difficult-to-deform metals, such as pure nickel and its alloys because of two core problems during metal extrusion, which limit the extrusion precision. The inevitable friction and wear at the billet-die interface produce large errors in the surface profile size of the workpiece [3,4]. Another issue is that the microstructure evolution mechanism is unclear due to the reorganization of the grain morphology.

Pure nickel has excellent corrosion resistance, high temperature resistance, and high temperature structural stability, so it is often used to manufacture pipes and bar components for the chemical and nuclear power industries [5,6]. Due to problems at high temperatures, such as a narrow processing window, difficult microstructure control, and serious die wear during the hot extrusion of pure nickel [7], warm extrusion is a better extrusion

Corresponding author: Zhi JIA, Tel: +86-18293167033, E-mail: jiazhi@lut.edu.cn;
De-xue LIU, Tel: +86-13919947009, E-mail: dxliu@lut.edu.cn
DOI: 10.1016/S1003-6326(23)66197-7

method for nickel alloys; however, wear, adhesion, fracture, grain refinement, texture evolution, and dislocation proliferation occur during this process [8]. The billet, die, and lubricant used during extrusion create a complex and variable plastic deformation friction system involving coupled process involving force, heat, and chemical reactions [9].

Three main research directions have been used to study friction and wear during extrusion, including field tests, ball-to-disk friction, and physical simulations [10−13]. However, field tests are the most essential method for studying the contact state of the billet-die interface. For instance, HILD et al [14] found that the maximum die wear during forward extrusion did not occur in the area with the highest interfacial pressure. Interfacial lubrication can improve the surface quality of workpieces during the hot extrusion of nickel-based superalloys [15]. The plastic deformation of nickel-based superalloy die is the main failure mode during hot extrusion [16]. Finite element simulation is an effective way to study extrusion. A combination of field tests and finite element simulations showed that lubrication had a great influence on extrusion friction [17]. The effect of lubrication on the extrusion of aluminum alloys was studied by changing the friction coefficient using finite element simulations [18].

There have already been reports of the microstructure of pure nickel and nickel alloys during thermal deformation, but most studies have used thermal compression and numerical simulations to study the microstructure evolution mechanism. For example, DANG et al [19] used Deform software to study changes in the interfacial temperature during nickel tube extrusion. The authors explored the dynamic recrystallization and texture evolution of Inconel 625 [20−22] and Inconel 617 [23] alloys during hot deformation and established a hot working model for nickel alloys. The precipitates in the nickel alloy during the hot deformation can hinder the grain growth and effectively improve the mechanical properties [24−26]. The grain distribution in the head, middle, and tail of the hot extruded nickel-based superalloy pipe was not uniform [27]. However, the grain morphology, grain boundary, texture evolution, dislocation, and deformation mechanism of pure nickel during warm extrusion have not been explained.

To sum up, there seem few reports on the evolution mechanism of surface defects and microstructure during the warm extrusion of pure nickel. In the present work, the surface and sub-surface defect morphologies of the workpieces were observed, and the surface wear mechanism during extrusion was studied. The grain morphology, the grain boundary distribution, the dislocation, and the texture evolution during the extrusion of pure nickel were analyzed, and the evolution process of the microstructure was explained.

2 Experimental

2.1 Specimen and extrusion

Commercial high-purity nickel N6 was used, whose composition is shown in Table 1. The original material was annealed under vacuum at 700 °C for 4 h to obtain an approximately equiaxed grain with improved plasticity. The original structure is shown in Fig. 1(a), where blue represents the recrystallized grains, and yellow represents the substructure. The orange circle represents the twin boundaries, whose calculated fraction was 40.3%. This showed that the original structure was composed of recrystallized grains with a large number of stable low-energy grain boundaries. The original material was cut into a cylinder (d10.5 mm × 20 mm) by wire cutting. The die material was H13 steel, and the extrusion ratio was 2.469. The physical drawing of the extrusion die is shown in Fig. 1(b). To reduce the friction between the billet and the die interface, 200$^{\#}$−1000$^{\#}$ sandpapers were used to grind the die and billet before extrusion. The surface morphology and two-dimensional profile of the original billet are shown in Fig. 1(d). Ultra-fine graphite powder lubricant was used to decrease the friction between the billet and the die during the extrusion processing. An electromagnetic induction coil with an optical temperature measurement heated the billet and die in two stages, and it was held for 20 min after reaching the specified temperature. The recrystallization temperature of pure nickel is about 600 °C [28]. To avoid promoting the recrystallization by the adiabatic heating effect [29], the warm extrusion temperatures were set as 100,

Table 1 Composition of pure nickel N6 (wt.%)

Ni + Co	Cu	Fe	Mn	C	Si	S	Al	Ti
99.6	0.064	0.11	0.05	0.047	0.018	0.045	0.046	0.018

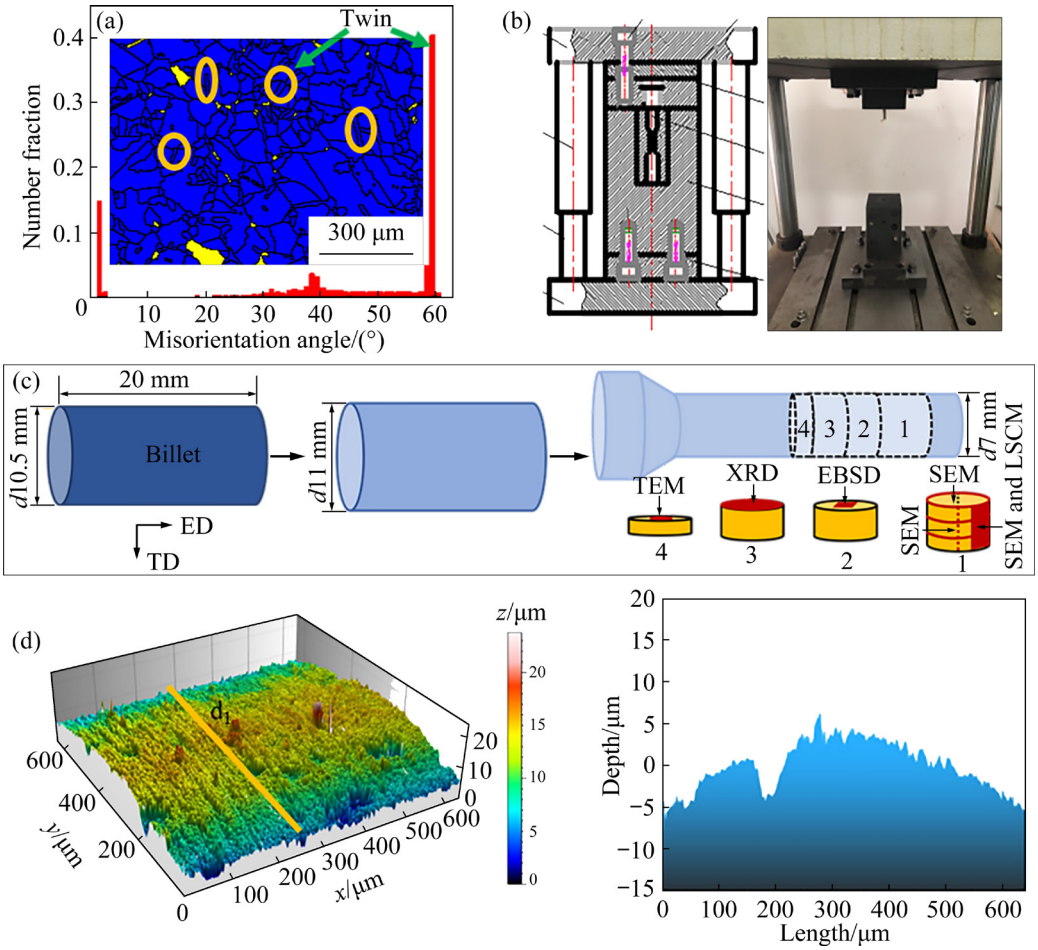

Fig. 1 Original structure of pure nickel and misorientation distribution (a), real images of extrusion (b), principle of extrusion and analysis (the red part in the picture is the observed area) (c), and original surface macro-morphology and two-dimensional profile (d)

200, 300, and 400 °C. Three sets of experiments were used to study the regularity of the surface morphology and microstructure evolution. A schematic diagram of the extrusion process is shown in Fig. 1(c).

2.2 XRD analysis

The pure nickel crystal structure was analyzed using a D8 ADVANCE X-ray diffractometer with a Cu target (λ=0.15406 nm). The scanning Bragg angle range was 30°−110°, and the step size was 0.02°.

2.3 Surface morphology observation

Because the contact state of each point of the billet displacement was different during extrusion, to reduce the sampling error, each analysis position was exactly the same, namely, the red region in Fig. 1(c). After sampling, ultrasonic cleaning was carried out in acetone solution for 10 min to prevent surface impurities from influencing the results. An LSM 800 laser scanning confocal microscope (LSCM) was used to analyze the three-dimensional morphology and two-dimensional profile of the sample surface. In the roughness test three sets of data were used to calculate the average value. A Quanta FEG−450 thermal field scanning electron microscope (SEM) was used to analyze the micromorphology of the sample surface, cross-section, and longitudinal section. Because the cross/longitudinal section information was occasional, they were observed at three different positions.

2.4 Microstructure analysis

Electron backscatter diffraction (EBSD) was used to analyze the microstructure, grain boundaries, and texture under a scanning step of 1 μm. A JEM−2010 transmission electron microscope (TEM) was used to observe the microstructure and dislocations of the cross-section. Before LSCM, SEM, EBSD, and XRD observations, samples were ground and polished with sandpaper. The TEM sample was firstly cut into slices with a thickness of 300 μm, then ground to a thickness of 50 μm with sandpaper, and finally processed into *d*3 mm slices with a Gatan 625 pit tester. The EBSD and TEM samples were electropolished and double-sprayed in a mixed solution of 90 vol.% C_2H_5OH and 10 vol.% $HClO_4$. The polishing voltage of the EBSD sample was 50 V, and the temperature was −20 °C. The double-spray voltage for the TEM sample was 22 V, and the temperature was about 0 °C. EBSD data were processed using Channel 5 software. In this work, EBSD counts high angle grain boundaries (HAGBs, θ>15°, black line), medium angle grain boundaries (MAGBs, 10°<θ<15°, green line), and low angle grain boundaries (LAGBs, 3°<θ<10°, red line).

2.5 Finite element simulations

Deform-3D software was used to simulate the pure nickel extrusion process. The billet type was a plastic body, and the die was a rigid body. To accurately simulate the deformation process, the mesh length of the billet was about 0.2. The shear friction model was used to define the complex interface between the billet and die. The heat exchange coefficient between the billet and the die was 11 N/(s·mm·℃), and the friction coefficient was 0.3. The temperature, stress, and strain distributions during the extrusion of pure nickel were analyzed in detail.

3 Results

During extrusion, the shape and microstructure of the workpiece change simultaneously due to friction heat and material deformation heat. Therefore, separately studying the surface defects or microstructure formation mechanism of the workpiece during pure nickel extrusion cannot account for coupling of the macro interface (surface) and the micro interface (grain boundary); thus, the obtained results typically have large errors.

3.1 Surface wear

Studying the surface morphology is an effective way to understand the contact state and wear mechanism of a sample. Changes in the surface morphology can largely explain the failure behavior of workpieces such as surface wear and fatigue.

3.1.1 Surface morphology characteristics

Figure 2 shows the three-dimensional macro-morphology and two-dimensional profile curves under extrusion at different temperatures, which provide the information of the horizontal plan and cross-section of the workpiece. It can be seen that the macroscopic morphology contains furrows of different sizes along the extrusion direction. Compared with the original billet morphology, extrusion can improve the surface quality. The surface was relatively smooth at 100 °C, but at 400 °C, surface material was lost, and pits were formed. As the temperature increased, the average surface roughness increased, and reached the maximum of 0.559 μm at 400 °C.

Figure 3 shows the micromorphology of the surface of the extruded workpiece. The wear surface morphology was different at various temperatures. At 100 °C, there were cracks and furrows on the surface along the extrusion direction, and steps and wear debris were found after magnifying an area (Figs. 3(a_1) and (a_2)), indicating fatigue wear. There was residual graphite lubricant in the cracks. As the extrusion progressed, the abrasive dust acted as an abrasive at the billet/die interface, and abrasive wear occurred, as shown by the yellow dotted line in Fig. 3. This showed that abrasive wear was induced by fatigue wear. A large number of pits (yellow circle in Fig. 3(b_1)) and abrasives were found on the extruded surface at 200 °C. This is a typical morphological feature of fatigue wear. Scales and furrows appeared on the surface of the extruded bar at 300 °C. The furrow morphology at 300 °C was more uniform than that at 100 and 200 °C, indicating that furrowing was continuous and stable. When the temperature reached 300 °C (Fig. 3(c)), the graphite lubricant may have been partially oxidized and failed, and the billet surface temperature rose and softened. The billet and the die part were in contact with each other. At this time, the abrasive was a hard asperity on the surface of the die, which was equivalent to micro-cutting. This is also a common form of

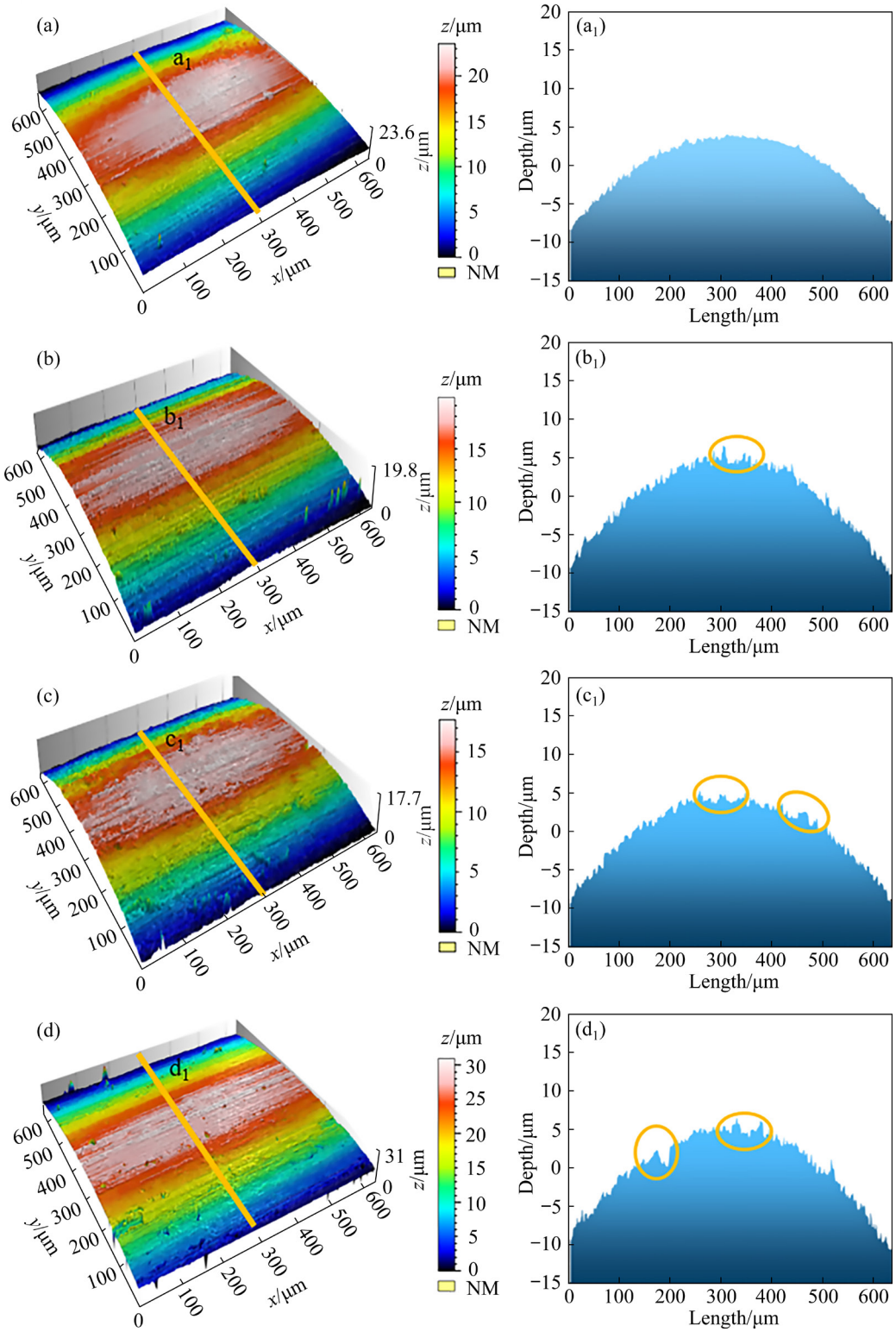

Fig. 2 Surface macro-morphology and two-dimensional profile at different temperatures: (a, a_1) 100 °C; (b, b_1) 200 °C; (c, c_1) 300 °C; (d, d_1) 400 °C

abrasive wear. During extrusion at 400 °C, the microscopic surface material of the rod flowed downwards like a river, and there were obvious cracks between the flowing material and the matrix (Fig. 3(d)). This indicated that the deformation of the surface material was not synchronous. The plasticity of the material was better at 400 °C, and the interfacial temperature was determined by the

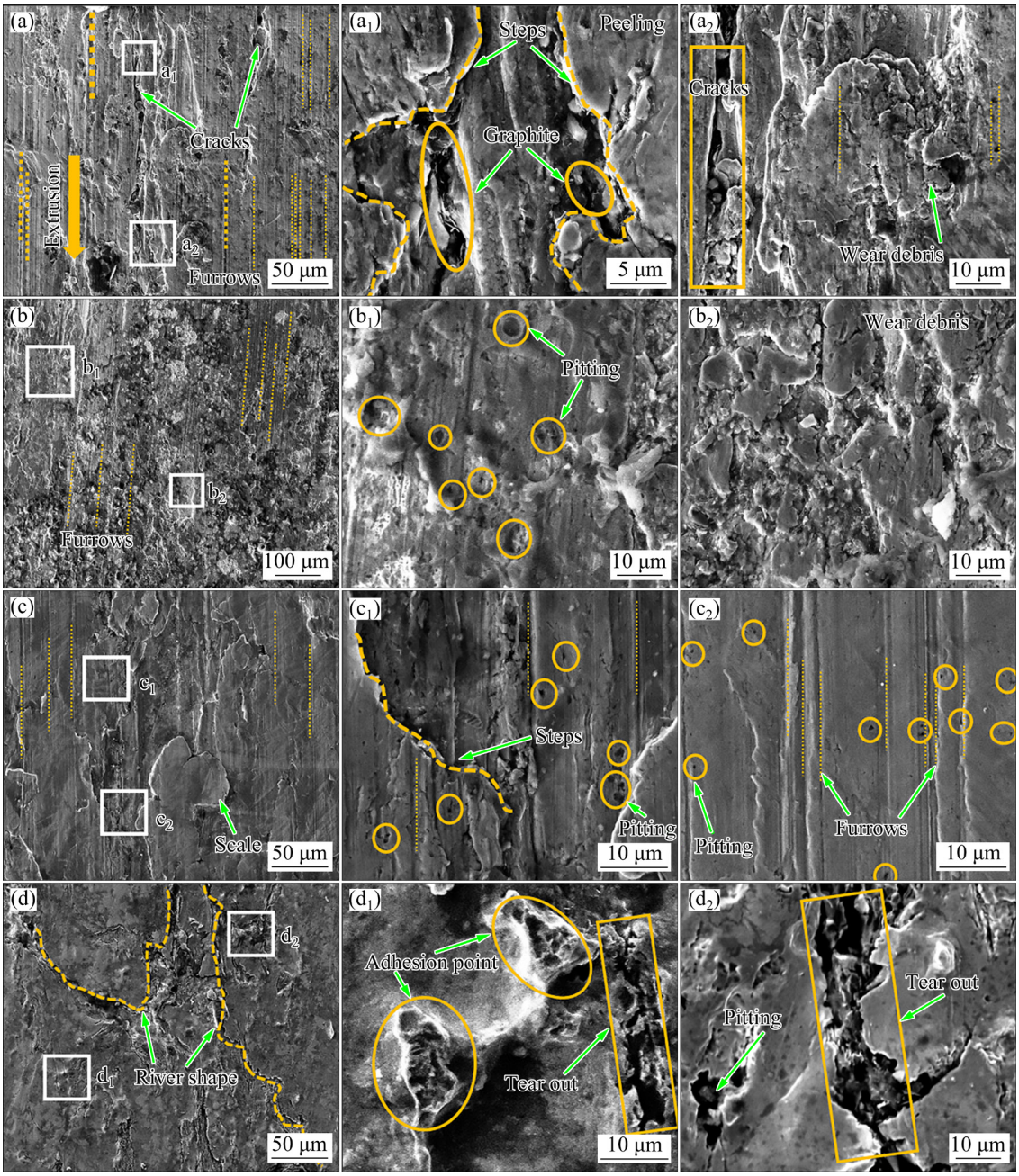

Fig. 3 SEM images of surface of extruded workpiece at different temperatures: (a, a_1, a_2) 100 °C; (b, b_1, b_2) 200 °C; (c, c_1, c_2) 300 °C; (d, d_1, d_2) 400 °C

billet temperature and the instantaneous temperature, and the real temperature was higher than the set temperature; therefore, the surface material was softer, and the fluidity was poorer in the area where the coefficient of friction with the billet was higher during extrusion. In high magnification SEM images, the surface material displayed adhesion points and pitting, indicating that adhesion wear and fatigue wear occurred. The seizure and tearing of the adhesion points damaged the surface material.

3.1.2 Section morphology characteristics

To better understand the causes of surface defects in the extruded bars, the cross-section and longitudinal section were analyzed, as shown in Fig. 4. Abrasive wear mainly occurred on the surface of the material, while the damage caused by fatigue wear and adhesive wear occurred on the subsurface. At a low temperature (100 °C), surface cracks appeared on the bar due to cyclic stress and work hardening. The cracks extended from surface defects to the interior angles of 10°−45° along the

extrusion direction; therefore, the loss of this material was defined as brittle damage. At a high temperature (400 °C), the surface material was relatively soft because the temperature offset work hardening to a certain extent. The asperity on the surface of the billet and die adhered due to contact stress, causing the surface material to tear along the extrusion direction. Subsequently, during extrusion, the interfacial lubricant (or the third body) and the rough peak of the die continued to cause damage, eventually causing large pieces of the material to peel off (Figs. 4(c, d)). This method of adhesion and tearing can be regarded as plastic damage, which showed that the extrusion temperature greatly influenced the damage mechanism of the surface.

3.2 Microstructure evolution

During plastic deformation, the grain size, high, medium, and low grain boundary fractions, substructure, dislocation density, and texture type changed. A detailed analysis was carried out on these factors.

3.2.1 Grain morphology and grain boundaries

The XRD diffraction patterns were mainly composed of peaks of five crystal planes: (111), (200), (220), (311), and (222) (Fig. 5(a)). No new diffraction peaks appeared during the extrusion process, indicating that no new phases were produced; however, the diffraction peak size was different under different conditions, and a slight shift occurred (Figs. 5(b) and (c)). The calculated lattice

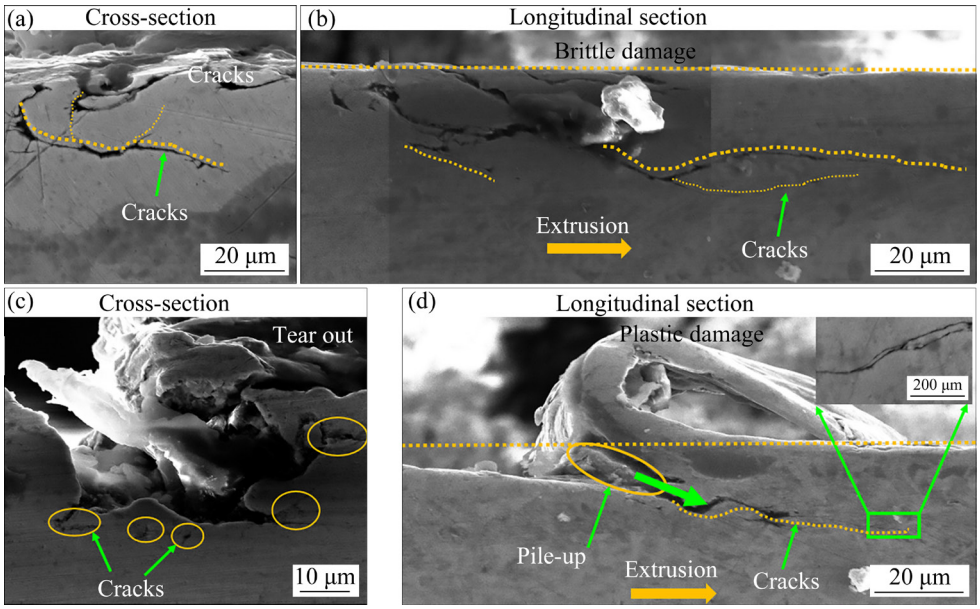

Fig. 4 SEM images of sections at 100 °C (a, b) and 400 °C (c, d)

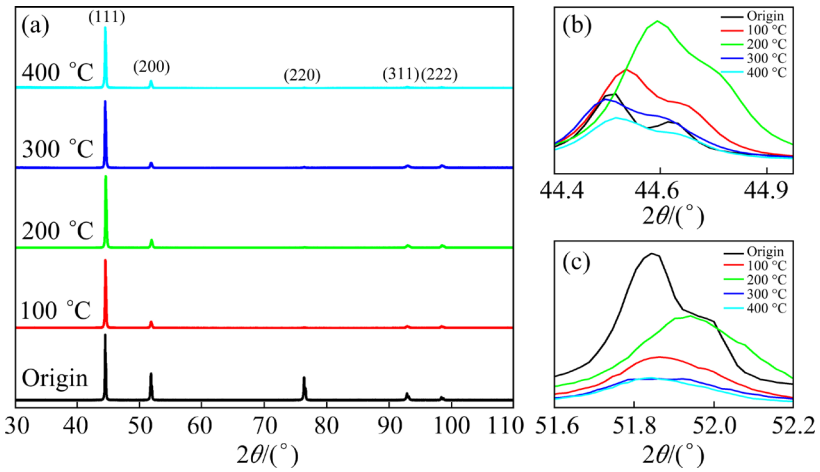

Fig. 5 XRD patterns of pure nickel (a) and diffraction peaks of (111) (b) and (200) (c) crystal planes at different extrusion temperatures

constant a of the sample at different extrusion temperatures fluctuated by ±0.005 Å. Changes in the lattice constant and the shift in the diffraction peaks occurred due to differences in the stress state and microstructure of the billet [30].

Figures 6(a) and (b) show the inverse pole figures of the sample, where different colors of the grains represent different orientations. In addition, the grain orientations were different and changed in a gradient along the elongation direction of the grains. The comparison showed that there were many HAGBs in pure nickel extruded at 100 °C, many fine grains gathered at large grain boundaries, and the grains were more evenly distributed than in the 400 °C sample. Upon increasing the extrusion temperature, the grain size gradually increased, but the increase was small, and the grain size was in the range of 3−4.2 μm.

It can be seen from Fig. 7(a) that a large number of LAGBs existed in the HAGBs, which were mainly caused by dislocations induced by plastic deformation. In addition, the LAGBs in different grains were arranged along a certain direction, indicating that the formation of LAGBs was closely related to changes in the grain orientation. The LAGBs were concentrated in the

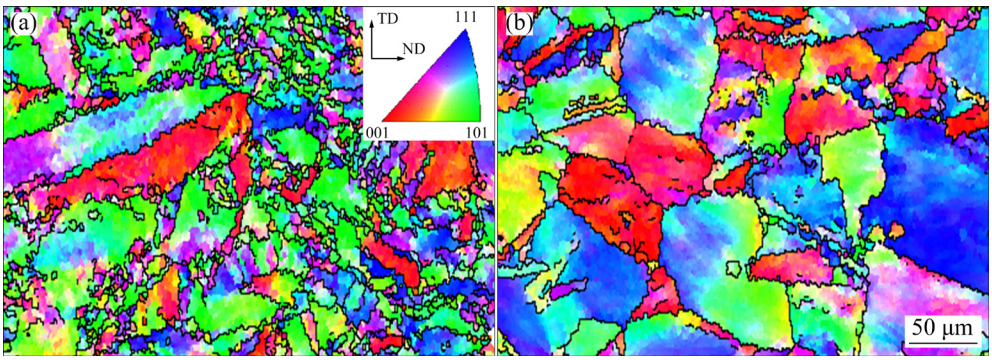

Fig. 6 Inverse pole figures of deformed sample at different temperatures: (a) 100 °C; (b) 400 °C

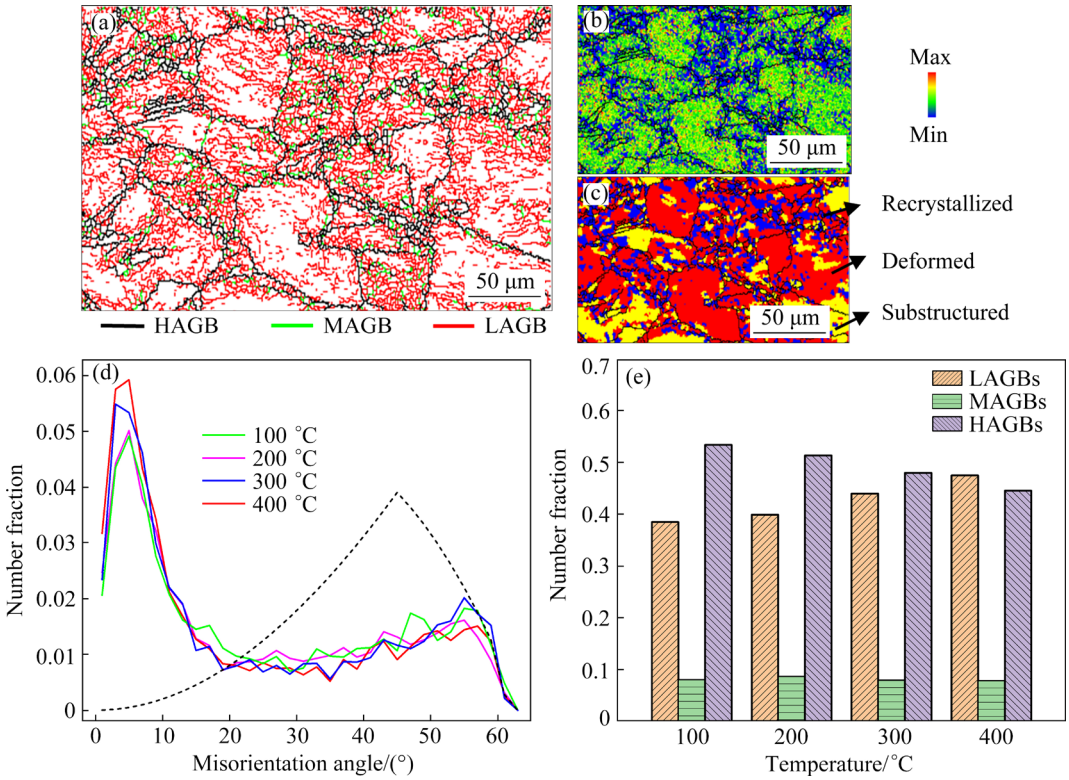

Fig. 7 Grain boundary distribution (a), KAM value (b), and grain type (c) of pure nickel extruded at 400 °C, misorientation distribution of samples extruded at different temperatures (d), and histogram showing number fractions of high, medium, and low grain boundary (e)

deformed grains and substructures, and the kernel average misorientation (KAM) value was relatively large. The smaller KAM value in the area with a small grain distribution indicated that the dislocation defects in this area were balanced and absorbed, and the strain was smaller. The MAGBs between LAGBs and HAGBs can be used to analyze the grain boundary transformation rate. The larger the fraction of MAGBs is, the faster the grain boundary transformation rate is. In Fig. 7(e), the MAGBs fraction was basically stable at about 8% at different extrusion temperatures. Interestingly, as the extrusion temperature increased, the LAGBs fraction increased, and the HAGBs fraction decreased. MAGBs gathered around small grain boundaries, which also showed that the generation of small grains occurred due to the evolution of LAGBs. The higher the extrusion temperature is, the smaller the average misorientation angle is. The dotted line in the Fig. 7(d) is the probability distribution curve of the misorientation of the cubic metal, i.e., the Mackenzie distribution [31]. Since the average misorientation angle was much smaller than the maximum orientation (45°) in the Mackenzie distribution, the structure of pure nickel was greatly refined by extrusion.

3.2.2 Layered structure and ultra-fine grains

According to EBSD observations, the grain orientation and LAGBs were highly-oriented, so the microstructure of pure nickel was analyzed by TEM. The results showed two main microstructures of pure nickel: a large number of layered structures (LSs) (Fig. 8) and a small number of ultra-fine grains (UFGs) (Fig. 9).

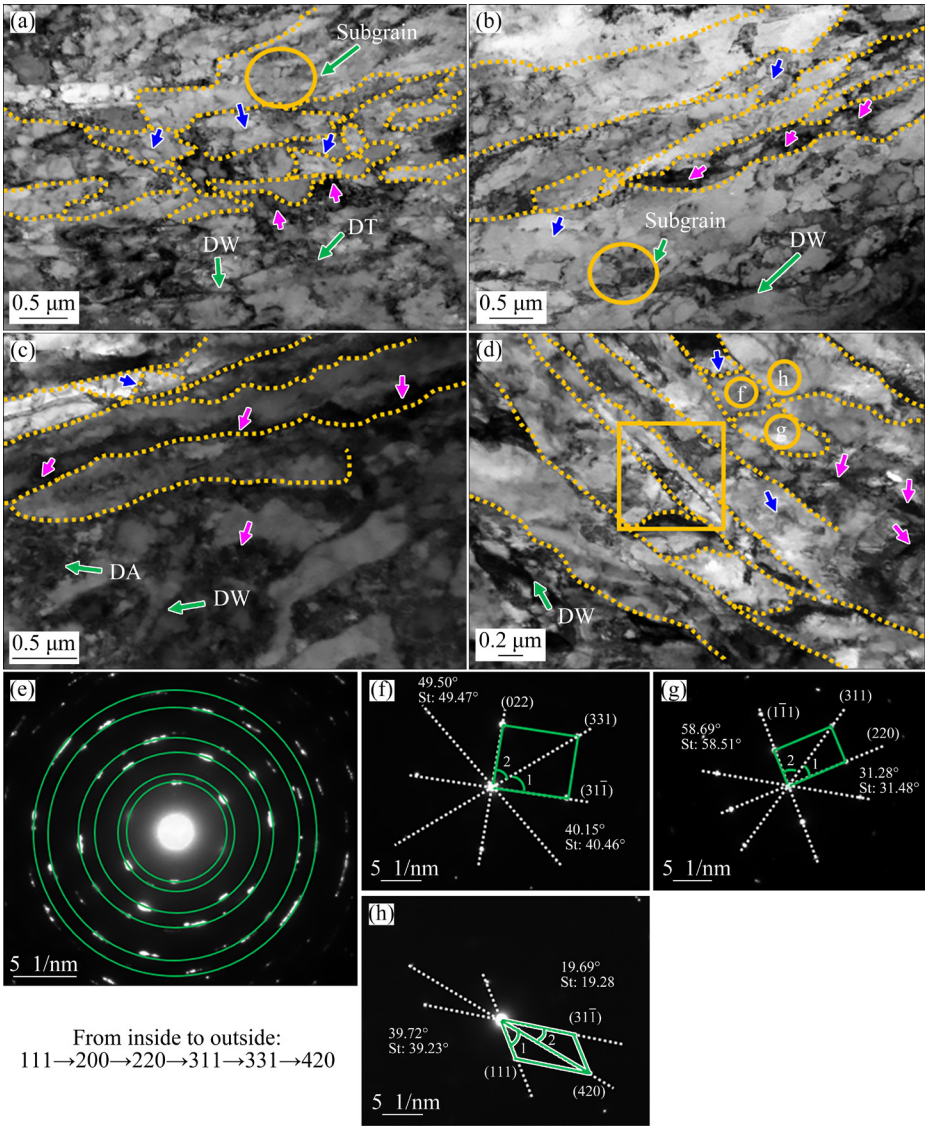

Fig. 8 BFTEM images of LS at 100 °C (a), 200 °C (b), 300 °C (c), 400 °C (d) and full (e), and partial SAED patterns (f, g, h) of (d)

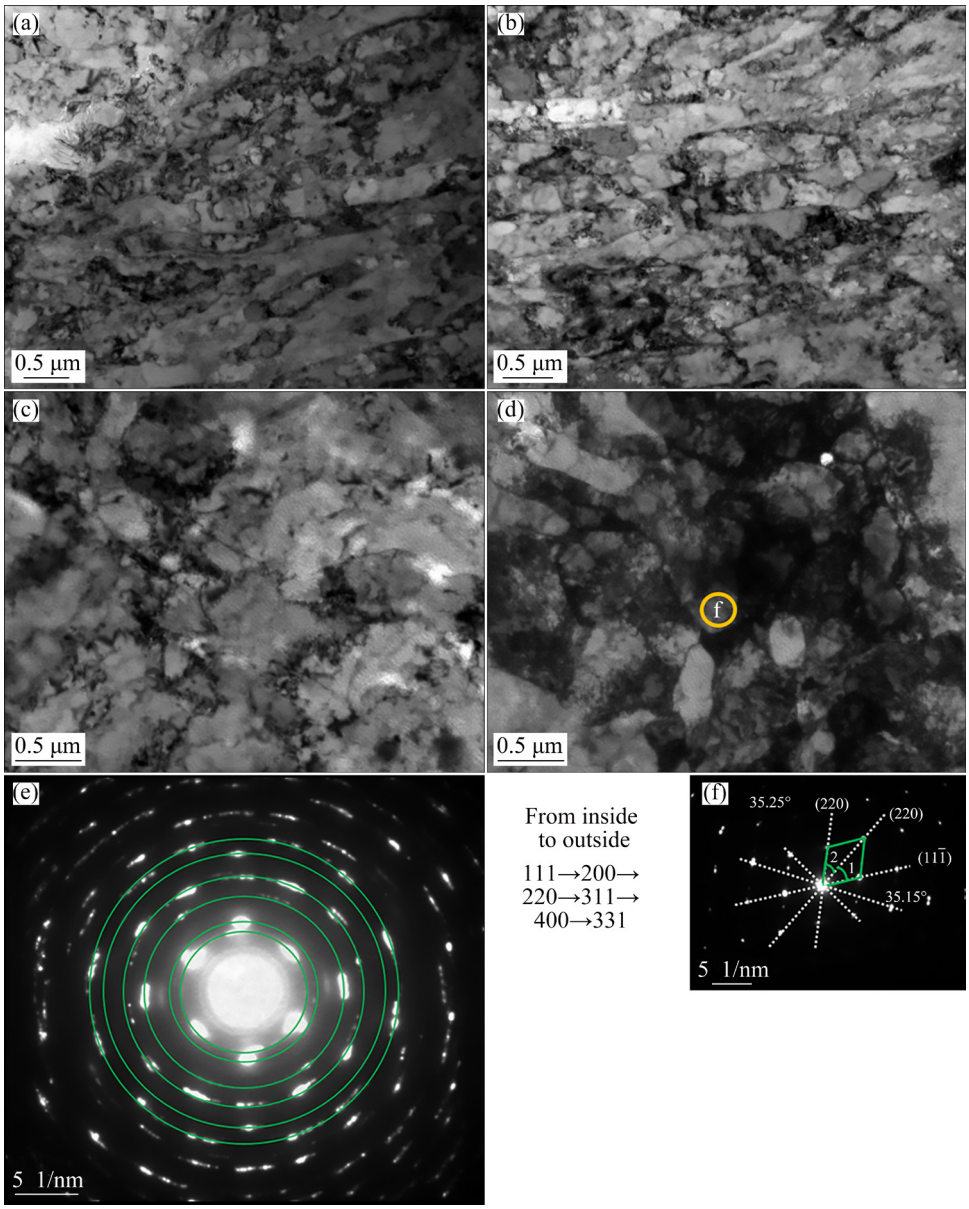

Fig. 9 BFTEM images of UFGs in samples extruded at 100 °C (a), 200 °C (b), 300 °C (c), 400 °C (d), and corresponding SAED patterns (e, f) of (d)

The long and flat thin layered substructure and the bamboo-like structure composed of dislocations are called the LS [30]. The LS obtained by bright-field transmission electron microscopy (BFTEM) is shown in Fig. 8. The LS may eventually directly affect the grain orientation gradient and the LAGBs arrangement. The isolated dislocations were approximately perpendicular to the LS boundary (the blue arrows in the figure) and finally split the LS into equiaxed substructures [32,33]. A large number of dislocation tangles (DT), dislocation aggregation (DA), dislocation cell (DC), and dislocation walls (DW) (purple arrows) were found in the inner and outer regions of the LS. As the extrusion temperature increased, the LS was widened. Figure 8(e) shows the corresponding selected area electron diffraction (SAED) of Fig. 8(d), which shows that the LS has already become polycrystalline. SAED analysis was performed on the substructures formed in the same LS and the substructures in the adjacent LS. The results showed that the orientation of the substructures was also different, which indicated that intragranular deformation was dominant during the extrusion of pure nickel.

The BFTEM images of the UFGs of pure nickel at different extrusion temperatures were shown in Fig. 9, which showed that a UFG structure

was formed due to further cross fracture of the LS. The size of the UFGs also increased with the extrusion temperature, which corresponded to the width of the LS. To determine the orientation relationship between the LS and UFGs, SAED analysis was also carried out on the UFGs of the pure nickel samples extruded at 400 °C. The results showed that the crystal planes calibrated to the strongest diffraction ring of UFGs and LS were different, indicating that the orientation of UFGs and LS changed. But the independent ultrafine crystals were single crystals (Fig. 9(f)), which was different from a previous report that showed that the orientation of the LS did not change during the conversion of UFGs [30].

3.2.3 Dislocation

From the above TEM and EBSD analysis, it can be seen that no deformation twins formed during the warm extrusion of pure nickel, indicating that the plastic deformation was controlled by dislocations. Thus, it is very important to analyze the dislocation defects in the grains.

Since the original sample was annealed, the original dislocation density was low. Figure 10 showed the grain dislocation defects of pure nickel bars, which were caused by extrusion deformation. The presence of dislocations produced significant lattice distortion, so dislocations must move and change their forms to reduce the storage energy. The analysis showed that a large number of concentrated dislocations were produced in the grains of pure nickel extruded at 100 °C (Fig. 10(a)) and 200 °C (Fig. 10(b)). As deformation continued, when the dislocation density increased to a certain value, these dislocations formed DW, DT, and DA. Dislocations overlapped in the form of DWs, eventually forming thick and long DWs. Large DWs continued to absorb dislocations. When a certain strain gradient was reached, the DWs began to bend and absorb more dislocations. Finally, the DW evolved into a LAGB. In contrast, during extrusion at high temperatures (Figs. 10(c) and (d)), some dislocations accumulated at HAGBs, producing strain gradients at grain boundaries. The yellow circle is the bow of the grain boundary induced by the strain gradient, but at the same time, intragranular dislocations also moved in the form of DWs. The dislocation boundaries were different at various temperatures because the temperature changed the crystal strain. In general, dislocations during pure nickel extrusion underwent coordinated plastic deformation.

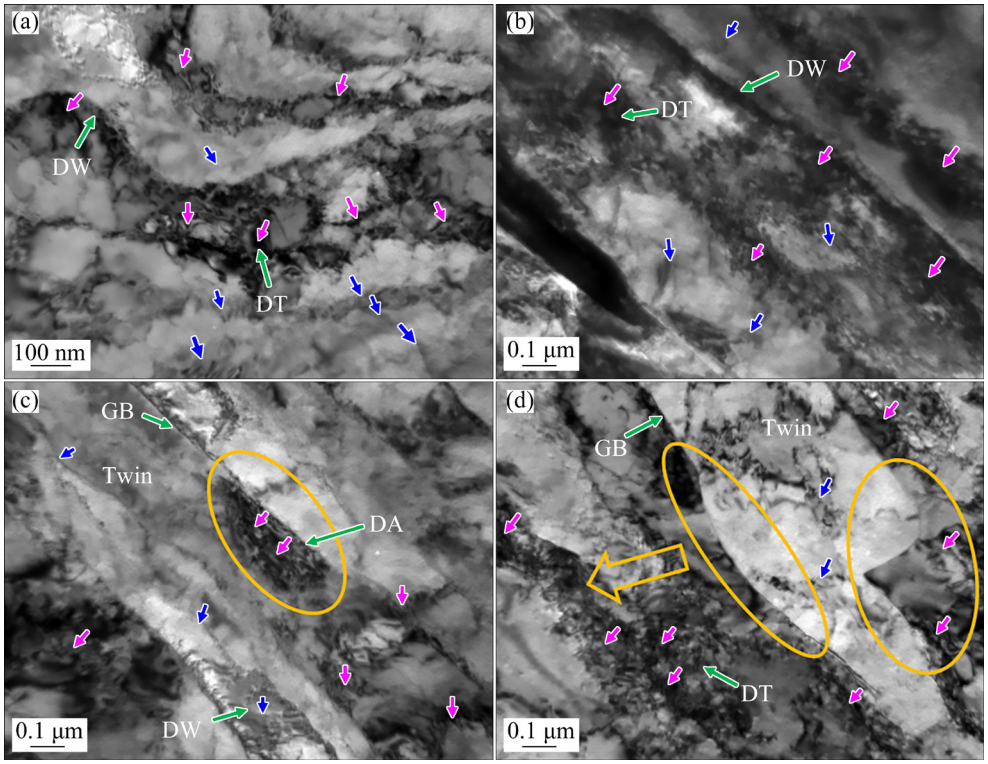

Fig. 10 BFTEM images showing dislocations in pure nickel extruded at different temperatures: (a) 100 °C; (b) 200 °C; (c) 300 °C; (d) 400 °C

According to continuum dislocation theory, dislocations produced to coordinate different polycrystalline strains are called geometrically necessary dislocations (GNDs) [34]. GNDs are directly related to the local misorientation θ, which can be quantitatively analyzed by the following formula [35,36]:

$$\rho^{\mathrm{GND}} = 2\theta/(ub) \quad (1)$$

where ρ^{GND} is the GND density; u is the unit length of a circle around a feature (that is, the scanning step length, 1 μm); b is the magnitude of Burgers vector (0.25 nm in this study); θ is obtained by KAM. The calculated GND density distribution histogram is shown in Fig. 11. The GND density fraction distribution firstly decreased, then increased, and finally decreased. Upon increasing the temperature, the minimum GND density fraction gradually increased, and the change was consistent with the LAGB fraction. The average GND densities of pure nickel extruded at 100 and 200 °C were 2.31×10^{14} m^{-2} and 2.30×10^{14} m^{-2}, respectively, which were higher than those obtained at 300 and 400 °C.

3.2.4 Texture

The original material was mainly composed of statically recrystallized grains due to the nucleation and growth of grains at randomly-oriented grain boundaries during annealing [37]. In face-centered cubic metals, the Euler space with φ_2 of 0°, 45°, and 65° is usually used to determine its texture composition. The black line to the purple line in the figure indicates that the orientation distribution function (ODF) value increased. Figure 12(a) shows the ODF figure of the original pure nickel, which shows that it is basically texture-free, but deformation created a strong texture. The results showed that some ideal textures formed mainly included copper{112}⟨111⟩, Brass{001}⟨211⟩, S{123}⟨634⟩, P{110}⟨122⟩, and Shear 2{111}⟨112⟩. The above-mentioned texture appeared during extrusion at both 100 and 200 °C; however, the different Shear 2 texture and deformation texture P were weak when extruded at 300 and 400 °C, which showed that the billet was subjected to a relatively small shearing force when extruded at >300 °C. This may be because the deformation resistance of the billet decreased when the temperature increased.

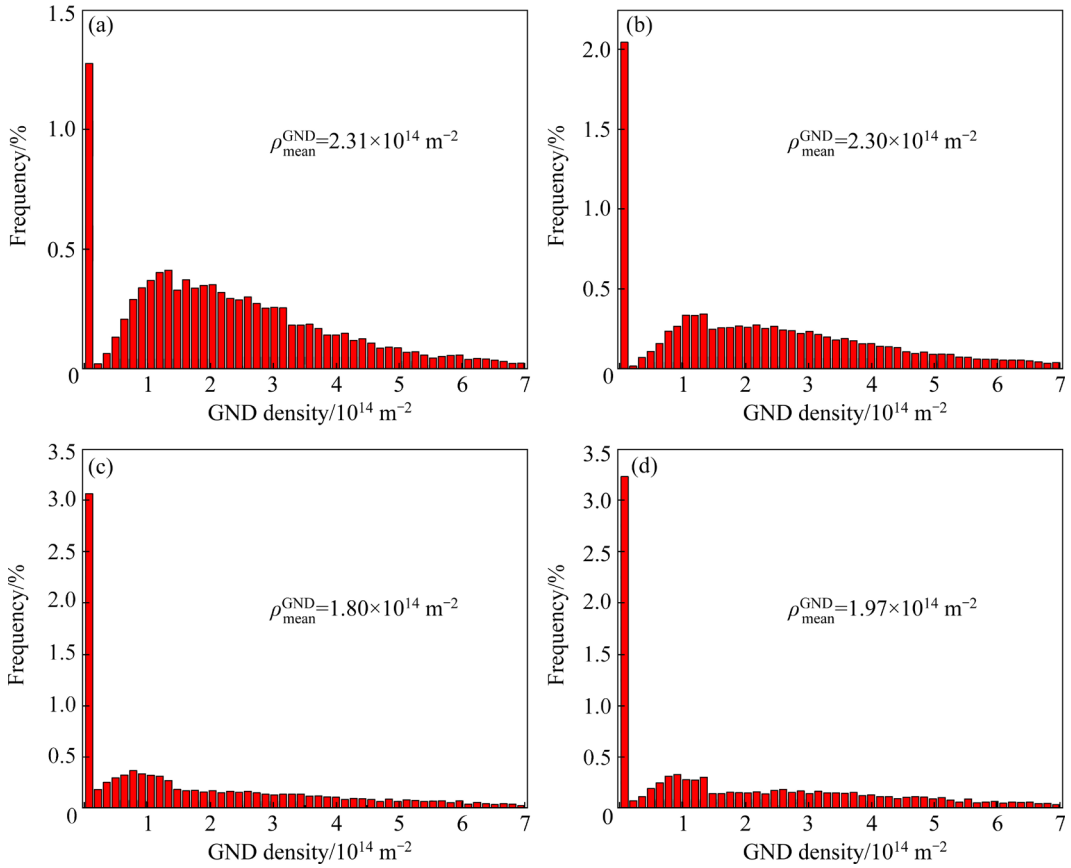

Fig. 11 Average GND density distribution of samples extruded at different temperatures: (a) 100 °C; (b) 200 °C; (c) 300 °C; (d) 400° C

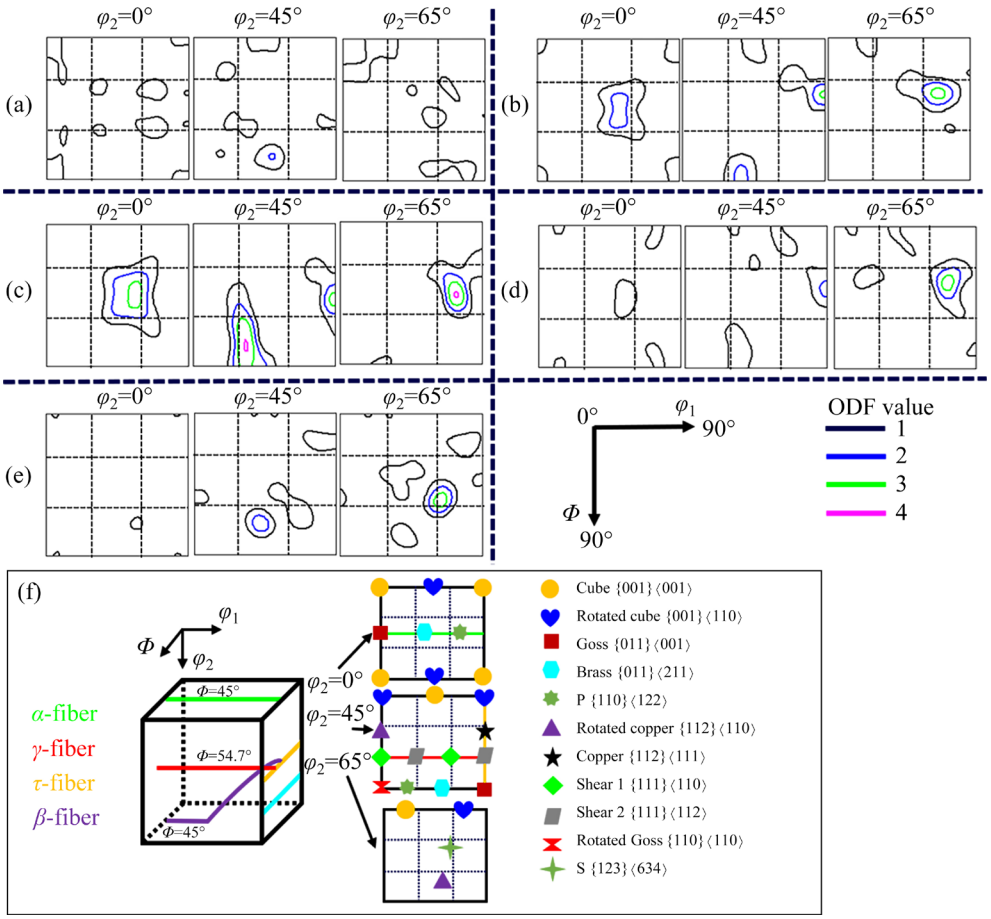

Fig. 12 Texture change on plane of φ_2=0°, 45°, and 65° in Euler space: (a) Original; (b) 100 °C; (c) 200 °C; (d) 300 °C; (e) 400 °C; (f) Position of special orientation fibers (α-fiber, β-fiber, γ-fiber, and τ-fiber) and standard texture in Euler space

Figure 13 showed the quantitative analysis of the orientation density of the microtexture during the extrusion of pure nickel. The microtexture on α-fiber, β-fiber, γ-fiber, and τ-fiber in Euler space was selected. There are mainly three kinds of textures on the α-fiber, where the grain orientation ⟨110⟩ was parallel to the normal direction (Fig. 13(a)), namely, Brass and P. As the temperature increased, the strength of the three textures on the α-fiber firstly increased and then decreased, and there was almost no texture at 400 °C. Figure 13(b) showed the β-fiber (φ_2= 45°−90°) in Euler space, which was inclined 60° from the normal direction to the extrusion direction. It can be found that as the temperature increased, the copper intensity gradually decreased, and the Brass intensity gradually increased; however, the S intensity firstly decreased and then increased with increasing temperature. There are Shear 1 and Shear 2 on the γ-fiber shown in Fig. 13(c). The strength of Shear 1 was always weak during warm extrusion, but as the temperature increased, the texture of Shear 2 changed to Shear 1. τ-fiber is often used to study the relationship between deformation twins and texture in metals with a low stacking fault energy [38]. The texture type shown in Fig. 13(d) was only copper, which also verified that twins did not appear during the warm extrusion of pure nickel.

4 Discussion

4.1 Wear mechanism

The surface wear behavior and microstructure evolution mechanism of pure nickel during warm extrusion are unclear. All tests showed that severe surface wear occurred during the warm extrusion of pure nickel, and the depth caused by wear was approximately 20 μm (Fig. 4). Simulations were performed on the temperature, stress, and strain of the workpiece, as shown in Fig. 14. The results showed a gradient change, and the maximum values

appeared on the surface. According to classical tribological theory, friction forces include adhesion forces (atomic or chemical action) and ploughing forces (asperity or abrasive particle action) [39]; therefore, the billet−die bearing interface stress is the key. Fatigue wear occurs during warm extrusion due to the action of cyclic changes in the contact stress, which causes the surface material to undergo work hardening and reduce the plasticity and stress concentration at some cutting marks and bumps. As a result, deformation (cracks and pitting in Fig. 3) occurred on the subsurface of the material, i.e.,

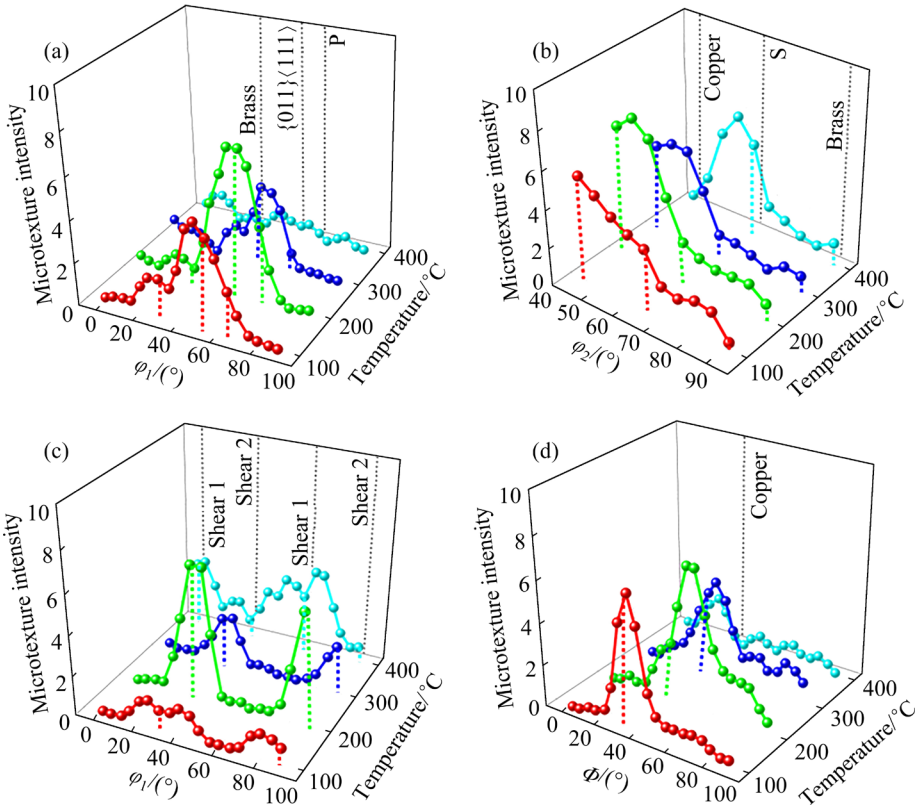

Fig. 13 Microtexture intensity at different extrusion temperatures on special orientation fibers in Euler space: (a) α-fiber; (b) β-fiber; (c) γ-fiber; (d) τ-fiber

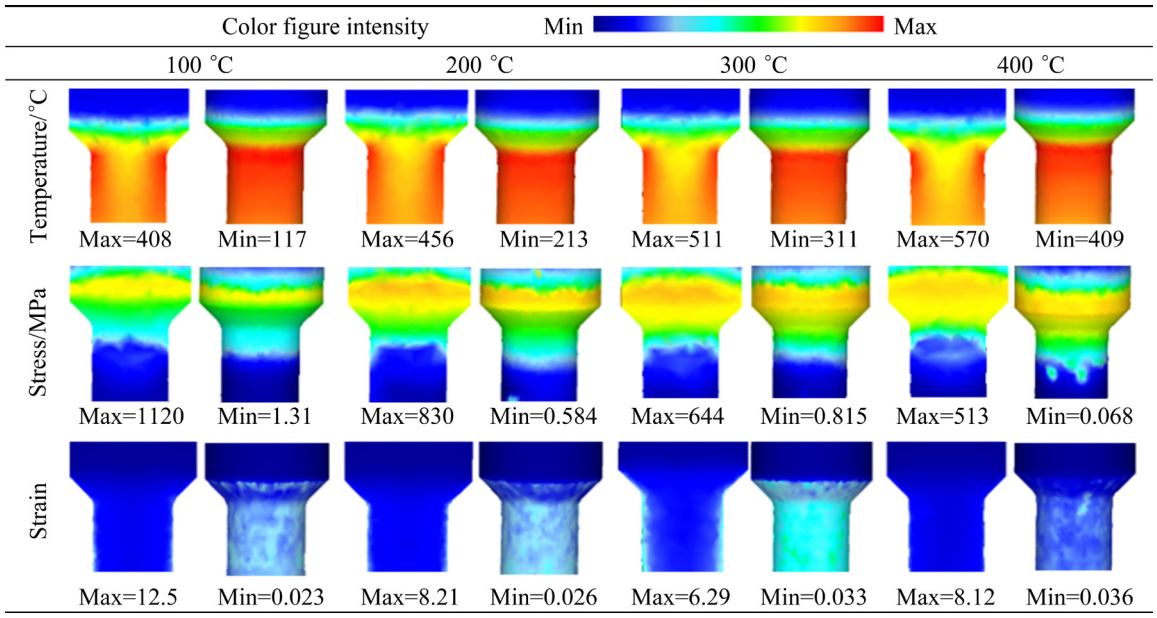

Fig. 14 Temperature, stress, and strain distributions of billet profile and surface at different extrusion temperatures

fatigue wear [40]. The difference was that fatigue cracks occurred at 100 °C, while pitting occurred at ≥200 °C because as the real temperature of the interface increased, the stress decreased, and the shearing force at the end of the asperity decreased so that cracks transformed into pits.

Abrasive wear also occurred during extrusion at ≤300 ℃, but the form of abrasive wear was different. At 100 and 200 °C, the third-body abrasive particles came from fatigue wear (Figs. 3(a) and (b)). The peeled-off material underwent the plastic deformation and strain strengthening after being ground at the billet−die interface. Due to the presence of abrasive particles, as extrusion progressed, extremely high contact stress was generated at the billet−die interface, which promoted the removal of surface material. As the temperature increased, the surface changed from brittle damage to plastic damage, and there were fewer abrasive particles on the surface of the wear scar. When extruded at 300 ℃, two-body abrasive wear was caused by hard asperities on the surface of the die penetrating into the surface of the billet. The wear morphology is shown as long and straight traces in Fig. 3(c). DELGADO-BRITO et al [41] reported that three-body abrasive wear was more serious than two-body abrasive wear.

The maximum real contact temperature reached 570 °C (about $0.35T_m$ of pure nickel) during extrusion at 400 °C. At this time, the interface asperities were softer, the contact area increased, and the adhesion effect occurred. There are two reasons for this. The atomic diffusion rate of the surface material was relatively high at high temperatures, and chemical interactions occurred where contact with asperities caused certain adhesive strength [42−45]. The diffusion rate of atoms can be expressed by Eq. (2) [46], and the adhesion strength can be expressed by Eq. (3) [39]:

$$D = D_0 \exp[-Q_D/(RT)] \tag{2}$$

$$f(T) = f_0 D[1-(T/T_m)]^{\eta} \tag{3}$$

where D is the billet−die mutual diffusion coefficient; Q_D is deformation activation energy; R is the molar gas constant; T is the true average contact temperature; $f(T)$ is the friction stress per unit area; f_0 is the average adhesive strength per unit area under a certain temperature as a reference; T_m is the melting point of pure nickel (1500−1600 °C); D_0 and η are constants.

The model showed that the adhesion effect was mainly controlled by the real interface temperature. As the temperature increased, the adhesive strength decreased, and the maximum shear stress on the surface also decreased; therefore, the wear process involves the discontinuous competition of asperities. When the shear force was greater than the adhesion force, the adhesion points tore and caused wear (Fig. 3(d) and Fig. 4(c)).

The temperature during metal plastic deformation largely determines the stress and strain; however, the study on the friction and wear behavior of pure nickel extrusion in this paper showed that the transformation of the wear mechanism also greatly influenced the stress and strain during material forming (Fig. 14). LIU et al [47] pointed out from the mechanism that the surface quality of extruded aluminum alloys was mainly related to abrasive particles. The difference is that the main factor that determines the surface quality of pure nickel (Fig. 2) is the wear mechanism (abrasive wear, adhesive wear, etc).

4.2 LS evolution mechanism

Figures 5, 6, 7, and 14 illustrate that as the true temperature increased and the stress decreased, the grain size and the LAGB fraction increased. The gradient distribution of temperature and stress during the warm extrusion of pure nickel likely dominated the microstructure evolution mechanism of LS. During deformation methods with gradient distributions of temperature or stress, such as laser shot peening [30], dynamic plastic deformation [48], rolling [49], etc, the LS also appears. This may be the deformation mechanism of pure nickel during plastic deformation at medium and low temperatures, but the gradient distribution of temperature and stress is affected by friction. The lower the temperature is and the greater the friction is, the greater the gradient distribution is and the narrower the LS is (Fig. 8). The cross-sectional area caused by wear is about 1% of the total area. Due to different wear mechanisms, the wear scar structure must be different [50,51], which may also be a reason for the deflection of the XRD peak in Fig. 3.

The LS formed mainly due to the movement and arrangement of dislocation walls. Figure 15 shows bright-field and dark-field TEM images of

the LS. The bright-field and dark-field images showed the entire spatial shape and distribution of dislocations. The following is an analysis of how dislocations moved to form the LS. LS in Fig. 15 was divided into 5 regions: (1) As extrusion progressed, a large number of dislocations began to appear. To reduce the distortion energy of the grains during deformation, dislocations within the grains spontaneously formed DWs. The high-density DW moved parallel to the (111) ⟨110⟩ slip system of pure nickel (i.e., perpendicular to the movement of the dislocation wall), which divided the original grain into layers; (2) Dislocations in the layered structure formed dislocation cells, LAGBs began to gradually form, and the dislocation density decreased [52]; (3) The existing defects in the original tissue acted as pre-nuclei that hindered dislocation [25]. The long and flat DWs formed a smaller LS, which was also why the III-zone LS was thinner than the surrounding structure; (4) Some scattered dislocations were similar to the dislocations in Zone II due to the introduction of LAGBs; (5) The layered structure with a low dislocation density was basical, and some isolated dislocations were rearranged perpendicularly to the LS. Finally, the interconnection split the layered structure and formed smaller sub-grains (Fig. 9).

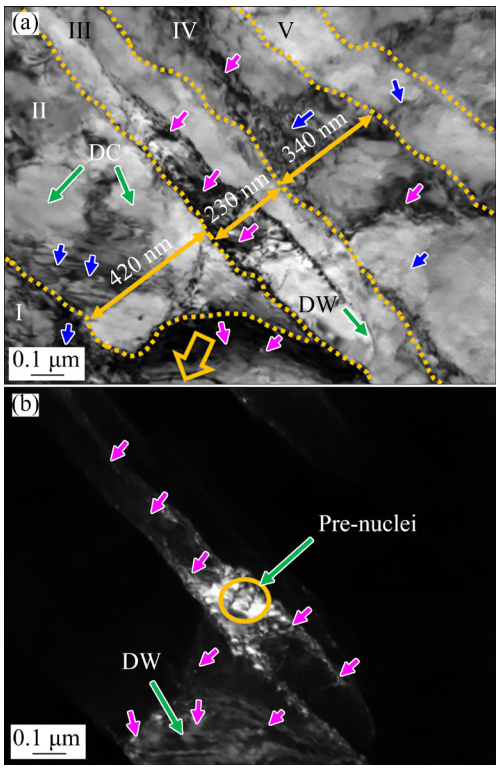

Fig. 15 Bright-field (a) and dark-field (b) TEM images of enlarged orange box in Fig. 8(d)

4.3 Main orientation grain characteristics

During pure nickel extrusion, deformation occurred due to normal and tangential forces, which produced a strong texture. The strength and type of texture greatly influenced the plastic strain capacity [53]. The five main ideal textures were identified in Fig. 12: P, S, Copper, Brass, and Shear 2. These were used to make the distribution map in Fig. 16. The chaotic interweaving of various textures showed that the textures underwent mutual transformation. The texture distribution was consistent with the LAGBs arrangement and the KAM distribution orientation gradient trends in Figs. 7(a) and (b). The movement arrangement of GNDs and the local migration rate of different grain boundaries resulted in a certain directionality in some grains [38]. That is, the dislocation wall shown in Fig. 10 is parallel to the specific (111) slip plane in the P, S, Copper, Brass, and Shear 2 orientation grains. WANG et al [38] also found that a texture was easily generated when the slip system was activated during the thermal deformation of the nickel alloy. According to the grain type determined in Fig. 7(c), the Schmidt factor (SF) values of the deformed grains were determined at different positions on the activated (111)⟨110⟩ slip system. It can be found that the SF value in the deformed grains was relatively large, and the average SF value reached 0.44, which showed that dislocations easily moved on the (111) slip plane. In addition, the SF within the same grain under this slip system changed greatly, indicating that the proliferation, recombination, and annihilation of dislocations were very active during extrusion. The grains that activated the slip system promoted the GNDs to form locally-ordered LS and also an ideal texture; therefore, slip transfer significantly improved the strain compatibility [54].

By analyzing the macromorphology and micromorphology of the workpiece surface and subsurface, it was concluded that there were multiple wear mechanisms at the interface during the warm extrusion of pure nickel. In order to better unify the expression of surface wear and microstructure evolution, the schematic diagram of showing wear mechanism and microstructure evolution in Fig. 17 was drawn.

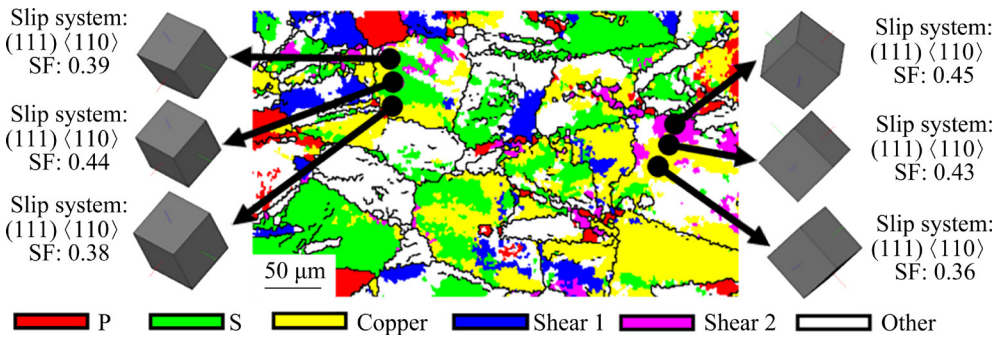

Fig. 16 Main texture distribution of pure nickel extruded at 400 °C

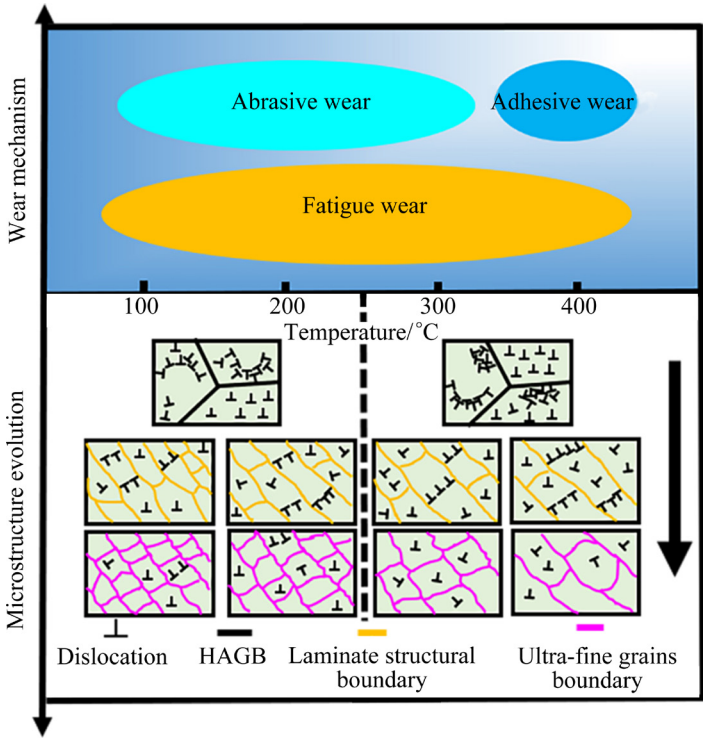

Fig. 17 Schematic diagram of surface wear mechanism and microstructure evolution during extrusion of pure nickel

5 Conclusions

(1) Fatigue wear occurred during extrusion at 100−400 ℃, in which fatigue cracks appeared at 100 ℃, and fatigue pitting occurred at ≥200 ℃. Fatigue wear during extrusion at 100 and 200 °C induced three-body abrasive wear. At 300 °C, two-body abrasive wear occurred due to the cutting action of die asperities. Adhesive wear occurred at 400 °C.

(2) During the extrusion of pure nickel, the long and straight dislocation walls transformed the original grain into LS on the activated slip system, and the isolated dislocations cut off the LS, and finally LAGBs were introduced.

(3) The lower the extrusion temperature, the greater the friction of the billet-die interface; thus, the more obvious the temperature and stress gradient distribution, and the narrower the LS.

(4) The GNDs in the deformed grain with a larger SF value formed an ideal texture (i.e., P, S, Copper, Brass, and Shear 2) on the (111) slip surface. At the same time, the grain had a larger strain gradient.

Acknowledgments

This work was financially supported by the Science Foundation for Distinguished Young Scholars of Gansu Province, China (No. 18JR3RA134), the Lanzhou University of Technology Support Plan for Excellent Young

Scholars, China (No. CGZH001), the National Nature Science Foundation of China (No. 51665032), and the Key R&D Program of Gansu Province−International Cooperation Project, China (No. 20YF8WA064).

References

[1] WANG L, HE Y, ZHANG Y, CAI J, ZHOU J, DUSZCZYK J, KATGERMAN L. Modeling of double action extrusion—A novel extrusion process for friction characterization at the billet—Die bearing interface [J]. Tribology International, 2010, 43: 2084−2091.

[2] FAN Qing, ZHOU Da-li, YANG Lei, ZHOU Jia-bei, YANG Shuang-qiao, YANG Yong-qiang. Study on the oxidation resistance and tribological behavior of glass lubricants used in hot extrusion of commercial purity titanium [J]. Colloids and Surfaces A: Physicochemical and Engineering Aspects, 2018, 559: 251−257.

[3] YU Zhi-qiang, ZHOU Gen-shu, TUO Lei-feng, SONG Cong-fei. Optimization of extrusion process parameters of Incoloy 028 alloy based on hot compression test and simulation [J]. Transactions of Nonferrous Metals Society of China, 2017, 27: 2464−2473.

[4] YUCEL B. Analysis of wear of a gas nitrided H13 tool steel die in aluminium extrusion [J]. Engineering Failure Analysis, 2012, 26: 203−210.

[5] WANG Chuan-jie, WANG Chun-ju, XU Jie, ZHANG Peng, SHAN De-bin, GUO Bin, WANG Zhen-long. Tensile deformation behaviors of pure nickel fine wire with a few grains across diameter [J]. Transactions of Nonferrous Metals Society of China, 2016, 26: 1765−1774.

[6] LIU Rui-yan, WANG Xu, ZHANG Jun-shan, WANG Xiu-min, ZHU Mei-li. Effect of borate coating on corrosion resistance of pure nickel in molten LiCl−Li_2O [J]. Transactions of Nonferrous Metals Society of China, 2004, 14: 143−147.

[7] HU Yong, WANG Xing-mao, GAO Yu-bi, XV Jia-yu, DING Yu-tian. Numerical simulation of effect of glass lubricant on hot extrusion of Inconel 625 alloy tubes [J]. Procedia Manufacturing, 2019, 37: 119−126.

[8] ZHOU Wen-bin, YU Jun-quan, LU Xiao-chen, LIN Jian-guo, DEAN T A. A comparative study on deformation mechanisms, microstructures and mechanical properties of wide thin-ribbed sections formed by sideways and forward extrusion [J]. International Journal of Machine Tools and Manufacture, 2021, 168: 103771.

[9] HU Ling-fei, GU Qin-fen, LI Qian, ZHANG Jie-yu, WU Guang-xin. Effect of extrusion temperature on microstructure, thermal conductivity and mechanical properties of a Mg−Ce−Zn−Zr alloy [J]. Journal of Alloys and Compounds, 2018, 741: 1222−1228.

[10] WANG L, ZHOU J, DUSZCZYK J, KATGERMAN L. Friction in aluminium extrusion. Part 1: A review of friction testing techniques for aluminium extrusion [J]. Tribology International, 2012, 56: 89−98.

[11] BIROL Y. High temperature sliding wear behaviour of Inconel 617 and Stellite 6 alloys [J]. Wear, 2010, 269: 664−671.

[12] YIN Cun-hong, LIANG Yi-long, LIANG Yu, LI Wei, YANG Ming. Formation of a self-lubricating layer by oxidation and solid-state amorphization of nano-lamellar microstructures during dry sliding wear tests [J]. Acta Materialia, 2019, 166: 208−220.

[13] MOSHKOVICH A, PERFILYEV V, BENDIKOV T, LAPSKER I, COHEN H, RAPOPORT L. Structural evolution in copper layers during sliding under different lubricant conditions [J]. Acta Materialia, 2010, 58: 4685−4692.

[14] HILD R, BERGS T, MATTFELD P, TRAUTH D, KLOCKE F, HOFFMANN D C, KRUPPE N C, BRÖGELMANN T, BOBZIN K. Analysis of wear phenomena during forward extrusion under dry friction conditions [J]. Wear, 2019, 426/427: 1362−1370.

[15] JIA Zhi, SUN Xuan, JI Jin-jin, WANG Yan-jiang, WEI Bao-lin, YU Li-dan. Effect of glass lubricant on the hot extrusion of Inconel 625 alloy [J]. Transactions of the Indian Institute of Metals, 2020, 73: 2795−2805.

[16] ANDERSON M J, MCGUIRE K, ZANTE R C, ION W J, ROSOCHOWSKI A, BROOKS J W. Identifying the dominant failure mode in the hot extrusion tooling used to forge nickel based superalloy [J]. Journal of Materials Processing Technology, 2013, 213: 111−119.

[17] HAFIS S M, RIDZUAN M J M, FARAHANA R N, AYOB A, SYAHRULLAI S. Paraffinic mineral oil lubrication for cold forward extrusion: Effect of lubricant quantity and friction [J]. Tribology International, 2013, 60: 111−115.

[18] JAYASEELAN V, KALAICHELVAN K, VIJAY A S. Lubrication effect on friction factor of AA6063 in forward extrusion process [J]. Procedia Manufacturing, 2014, 97: 166−171.

[19] DANG Li, YANG He, GUO Liang-gang, ZENG Wen-da, ZHANG Jun. Study on exit temperature evolution during extrusion for large-scale thick-walled Inconel 625 pipe by FE simulation [J]. The International Journal of Advanced Manufacturing Technology, 2015, 76: 1421−1435.

[20] JIA Zhi, GAO Ze-xi, JI Jin-jin, LIU De-xue, GUO Ting-biao, DING Yu-tian. High-temperature deformation behavior and processing map of the as-cast Inconel 625 alloy [J]. Rare Metals, 2021, 40: 2083−2091.

[21] JIA Zhi, GAO Ze-xi, JI Jin-jin, LIU De-xue, GUO Ting-biao, DING Yu-tian. Study of the dynamic recrystallization process of the Inconel 625 alloy at a high strain rate [J]. Materials, 2019, 12: 510.

[22] JIA Zhi, GAO Ze-xi, JI Jin-jin, LIU De-xue, GUO Ting-biao, DING Yu-tian. Evolution of twin boundaries and contribution to dynamic recrystallization and grain growth of Inconel 625 [J]. Advanced Engineering Materials, 2019, 21: 1900426.

[23] JIA Zhi, YU Li-dan, WEI Bao-lin, SUN Xuan, WANG Yan-jiang, LIU De-xue, DING Yu-tian. Effect of Temperature and strain rate on dynamic recrystallization of Inconel 617 during hot deformation [J]. Advanced Engineering Materials, 2021, 23: 2100493.

[24] GUO Yan, ZHANG Zhou-bo, ZHOU Rong-can, HOU Shu-fang, WANG Bo-han. Microstructure and mechanical

properties of alloy 617B [J]. Transactions of Nonferrous Metals Society of China, 2015, 25: 1106−1113.

[25] LIN Yong-cheng, HE Min, CHEN Ming-song, WEN Dong-xu, CHEN Jian. Effects of initial δ phase (Ni_3Nb) on hot tensile deformation behaviors and material constants of Ni-based superalloy [J]. Transactions of Nonferrous Metals Society of China, 2016, 26: 107−117.

[26] LIU Chen-ze, LIU Feng, HUANG Lan, JIANG Liang. Effect of hot extrusion and heat treatment on microstructure of nickel-base superalloy [J]. Transactions of Nonferrous Metals Society of China, 2014, 24: 2544−2553.

[27] GUO Qing-miao, LI De-fu, GUO Sheng, XIE Guo-ling. Hot deformation behavior and microstructure evolution of GH625 superalloy tube during extrusion process [J]. Advanced Materials Research, 2011, 1335: 640−644.

[28] ZHANG Bing, ZHU Le-le, WANG Kuai-she, WANG Wen, HAO Ya-xin. High temperature plastic deformation behavior and constitutive equation of pure nickel [J]. Chinese Journal of Rare Metals, 2015, 39: 406−413. (in Chinese)

[29] JIA Zhi, GAO Ze-xi, JI Jin-jin. A mechanism for the evolution of hot compression cracking in Inconel 625 alloy ingot with respect to grain growth [J]. Advanced Engineering Materials, 2020, 22: 1901445.

[30] CHEN Lan, REN Xu-dong, ZHOU Wang-fan, TONG Zhao-peng, ADU-GYAMFI S, YE Yun-xia, REN Yun-peng. Evolution of microstructure and grain refinement mechanism of pure nickel induced by laser shock peening [J]. Materials Science and Engineering A, 2018, 728: 20−29.

[31] QU Jing-long, XIE Xing-fei, BI Zhong-nan, DU Jin-hui, ZHANG Mai-cang. Hot deformation characteristics and dynamic recrystallization mechanism of GH4730 Ni-based superalloy [J]. Journal of Alloys and Compounds, 2019, 785: 918−924.

[32] SASAKI T T, YAMAMOTO K, HONMA T, KAMADO S, HONO K. A high-strength Mg–Sn–Zn–Al alloy extruded at low temperature [J]. Scripta Materialia, 2008, 59: 1111−1114.

[33] CHENG W L, KIM H S, YOU B S, KOO B H, PARK S S. Strength and ductility of novel Mg–8Sn–1Al–1Zn alloys extruded at different speeds [J]. Materials Letters, 2011, 65: 1525−1527.

[34] WANG Xin-yun, SHEN Bo, DENG Lei, LI Jian-jun. Effects of original orientation combination on substructure characteristics during continuous dynamic recrystallization in an extruded Al−Cu−Li alloy [J]. Materials Characterization, 2017, 130: 113−122.

[35] KUBIN L P, MORTENSEN A. Geometrically necessary dislocations and strain-gradient plasticity: A few critical issues [J]. Scripta Materialia, 2003, 48: 119−125.

[36] GAO H, HUANG Y, NIX W D, HUTCHINSON J W. Mechanism-based strain gradient plasticity—I. Theory [J]. Journal of the Mechanics and Physics of Solids, 1999, 47: 1239−1263.

[37] CHEN Jian-jun, DING Yu-tian, GAO Yu-bi, MA Yuan-jun, WANG Xing-mao, YAN Kang. Static recrystallization behavior of deformation induced Inconel 625 superalloy pipe [J]. Rare Metal Materials and Engineering, 2021, 50: 14−22.

[38] WANG M J, SUN C Y, FU M W, LIU Z L, WANG C H. Microstructure and microtexture evolution of dynamic recrystallization during hot deformation of a nickel-based superalloy [J]. Materials & Design, 2020, 188: 108429.

[39] WANG L L, ZHOU J, DUSZCZYK J, KATGERMAN L. Identification of a friction model for the bearing channel of hot aluminium extrusion dies by using ball-on-disc tests [J]. Tribology International, 2012, 50: 66−75.

[40] GÖK M S, KÜÇÜK Y, ERDOĞAN A, ÖGE M, KANCA E, GÜNEN A. Dry sliding wear behavior of borided hot-work tool steel at elevated temperatures [J]. Surface and Coatings Technology, 2017, 328: 54−62.

[41] DELGADO-BRITO A M, CONTLA-PACHECO A D, CASTREJÓN-SÁNCHEZ V H, LÓPEZ-SUERO D, OSEGUERA-PEÑA J, CAMPOS-SILVA I. Effect of the diffusion annealing process on the sliding wear resistance of cobalt boride layer [J]. Journal of Materials Engineering and Performance, 2020, 29: 109−125.

[42] BJÖRK T, BERGSTRÖM J, HOGMARK S. Tribological simulation of aluminum hot extrusion [J]. Wear, 1999, 224: 216−225.

[43] BJÖRK T, WESTERGÅRD R, HOGMARK S, BERGSTRÖM J, HEDENQVIST P. Physical vapour deposition duplex coatings for aluminium extrusion dies [J]. Wear, 1999, 225/226/227/228/229: 1123−1130.

[44] GUTOVSKAYA J, SOLBERG J K, LANGE H I, ANDERSEN L H. Wear of Inconel 718 die during aluminium extrusion—A case study [J]. Wear, 2004, 256: 126−132.

[45] WANG Yan-jiang, ZHAO Si-xiang, JIA Zhi, JI Jin-jin, LIU De-xue, GUO Ting-biao, DING Yu-tian. Study on friction and wear behavior of Inconel 625 superalloy during hot extrusion [J]. Advances in Materials Science and Engineering, 2020, 2020: 5453703.

[46] GHOSH M, BHANUMURTHY K, KALE G B, KRISHNAN J, CHATTERJEE S. Diffusion bonding of titanium to 304 stainless steel [J]. Journal of Nuclear Materials, 2003, 322: 235−241.

[47] LIU Zhi-wen, LI Li-luo, ZHANG Ming, LI Shi-kang. Research progress of interface friction in hot extrusion of aluminium alloys [J]. The Chinese Journal of Nonferrous Metals, 2017, 27: 1311−1322. (in Chinese)

[48] LUO Z P, ZHANG H W, HANSEN N, LU K. Quantification of the microstructures of high purity nickel subjected to dynamic plastic deformation [J]. Acta Materialia, 2012, 60: 1322−1333.

[49] HUGHES D A, HANSEN N. Microstructure and strength of nickel at large strains [J]. Acta Materialia, 2000, 48: 2985−3004.

[50] XU Y L, RUEBELING F, BALINT D, GREINER C, DINI D. On the origin of microstructural discontinuities in sliding contacts: A discrete dislocation plasticity analysis [J]. International Journal of Plasticity, 2021, 138: 102942.

[51] JIA Yan-jun, CHEN Han-ning, LIANG Xiao-dan. Microstructure and wear resistance of CoCrNbNiW high-entropy alloy coating prepared by laser melting deposition [J]. Rare Metals, 2019, 38: 1153−1159.

[52] YE C, SUSLOV S, FEI X L, CHENG G J. Bimodal nanocrystallization of NiTi shape memory alloy by laser shock peening and post-deformation annealing [J]. Acta Materialia, 2011, 59: 7219−7227.

[53] PAN H C, QIN G W, HUANG Y M, REN Y P, SHA X C, HAN X D, LI C F, WU X L, CHEN H W, HE C, CHAI L J, WANG Y Z. Development of low-alloyed and rare-earth-free magnesium alloys having ultra-high strength [J]. Acta Materialia, 2018, 149: 350−363.
[54] LI J L, WU D, CHEN R S, HAN E H. Anomalous effects of strain rate on the room-temperature ductility of a cast Mg−Gd−Y−Zr alloy [J]. Acta Materialia, 2018, 159: 31−45.

纯镍挤压制造过程中的磨损行为和显微组织演变

汪彦江[1,2]，贾 智[1,2]，姬金金[3]，魏保林[1,2]，衡亚博[1,2]，刘德学[1,2]

1. 兰州理工大学 省部共建有色金属先进加工与再利用国家重点实验室，兰州 730050；
2. 兰州理工大学 材料科学与工程学院，兰州 730050；
3. 兰州工业学院 材料工程学院，兰州 730050

摘 要：挤压棒材表面形貌和显微组织是决定其力学性能的主要因素。本文作者采用现场挤压和有限元模拟相结合的方法，研究挤压工件的表面磨损行为及显微组织演化机制。结果表明，挤压温度对合金的表面形貌和显微组织有很大的影响。随着挤压温度的升高，磨损机制由磨粒磨损(脆性损伤)转变为粘着磨损(塑性损伤)，并且表面粗糙度逐渐增大。挤压过程中坯料的温度和应力呈梯度分布，变形晶粒中的位错墙在激活的滑移系上运动，这导致层状结构产生变形。随着坯料梯度分布幅度和界面摩擦力的增大，层状结构变窄。此外，变形晶粒内几何必要位错的取向梯度也主导 5 种强理想织构。这些结果为纯镍及镍合金的精确挤压提供了理论依据。

关键词：纯镍；温挤压；磨损机制；层状结构

(Edited by Wei-ping CHEN)